

**SYNTHESIS AND CHARACTERIZATION OF  
BLACK SILICON BY SILVER-ASSISTED  
CHEMICAL ETCHING FOR SOLAR CELL**

**NUR AFIDAH BINTI MD. NOOR**

**UNIVERSITI SAINS MALAYSIA**

**2021**

**SYNTHESIS AND CHARACTERIZATION OF  
BLACK SILICON BY SILVER-ASSISTED  
CHEMICAL ETCHING FOR SOLAR CELL**

by

**NUR AFIDAH BINTI MD. NOOR**

**Thesis submitted in fulfilment of the requirements  
for the degree of  
Master of Science**

**March 2021**

## ACKNOWLEDGEMENT

First of all, I would like to express my deepest gratitude to my main supervisor; Dr. Mohd Zamir bin Pakhuruddin, for providing me with the opportunity to pursue this research under his supervision. His expertise in every aspect of photovoltaics (PV) has helped me to finish this thesis. Thanks for giving me a lot of guidance from designing my experiments until my thesis completion. Secondly, I would like to thank my co-supervisor, Professor Dr. Md. Roslan bin Hashim and my previous co-supervisor who has left Universiti Sains Malaysia (USM); Professor Dr. Mutharasu Devarajan for giving me useful advices.

Besides, I am deeply indebted to En. Yushamdan bin Yusof (Research Officer), Ms. Ee Bee Choo and Mr. Abd Jamil bin Yusuf as Assistance Science Officers at Nano-Optoelectronics Research and Technology (NOR) laboratory, School of Physics, for giving me trainings to use lab equipments. Without your help and patience, all my experiments would not be possible. I also would like to extend my sincere appreciation to the members of Photovoltaic Materials and Devices (PVMD) group, particularly for those who work on black silicon solar cells. I really owe them a huge acknowledgement because of their immense support throughout my MSc journey. Thank you for being patient with me throughout this journey. I feel so grateful to be in the team.

## TABLE OF CONTENTS

<b>ACKNOWLEDGEMENT</b> .....	<b>ii</b>
<b>TABLE OF CONTENTS</b> .....	<b>iii</b>
<b>LIST OF TABLES</b> .....	<b>vi</b>
<b>LIST OF FIGURES</b> .....	<b>viii</b>
<b>LIST OF SYMBOLS</b> .....	<b>xiv</b>
<b>LIST OF ABBREVIATIONS</b> .....	<b>xv</b>
<b>ABSTRAK</b> .....	<b>xvii</b>
<b>ABSTRACT</b> .....	<b>xix</b>
<b>CHAPTER 1 INTRODUCTION</b> .....	<b>1</b>
1.1 Background .....	1
1.2 Problem statement .....	2
1.3 Objectives.....	5
1.4 Thesis outlines.....	5
<b>CHAPTER 2 LITERATURE REVIEW</b> .....	<b>7</b>
2.1 Introduction .....	7
2.2 Solar radiation .....	7
2.3 Light trapping .....	9
2.4 Black silicon .....	12
2.4.1 Fabrication methods of black silicon .....	14
2.4.2 Mechanism of two-step metal-assisted chemical etching.....	17
<b>CHAPTER 3 METHODOLOGY</b> .....	<b>21</b>
3.1 Introduction .....	21
3.2 Fabrication of black silicon .....	21
3.2.1 RCA cleaning.....	22

3.2.2	RF sputtering.....	23
3.2.3	Annealing.....	24
3.2.4	Etching.....	25
3.3	Characterization of black silicon.....	27
3.3.1	Atomic Force Microscopy .....	28
3.3.2	Field Emission Scanning Microscopy and Energy Dispersive X-Ray Spectrophotometer .....	29
3.3.3	UV-Vis-NIR spectrophotometer.....	30
3.4	Fabrication of homojunction black silicon solar cell .....	33
3.4.1	Spin coat .....	33
3.4.2	Diffusion .....	34
3.4.3	Thermal evaporation.....	35
3.5	Characterization of homojunction black silicon solar cell.....	37
3.5.1	Hall effect .....	37
3.5.2	Solar simulator – White LED System.....	39
<b>CHAPTER 4 RESULTS AND DISCUSSIONS.....</b>		<b>42</b>
4.1	Introduction .....	42
4.2	Effects of etching time .....	42
4.2.1	Morphological properties.....	43
4.2.2	Optical properties.....	47
4.3	Effect of etchant volume ratio .....	52
4.3.1	DI H <sub>2</sub> O .....	52
4.3.2	HF and H <sub>2</sub> O <sub>2</sub> .....	61
4.4	Effects of annealing temperature.....	71
4.4.1	Morphological properties.....	73
4.4.2	Optical properties.....	76
4.5	Cross section of optimized b-Si wafer .....	82
4.6	Morphological properties of P-N junction .....	85

4.7	Optical properties of doped silicon .....	87
4.8	Electrical properties of PN junction .....	90
4.9	Light I-V measurement .....	91
<b>CHAPTER 5 CONCLUSIONS AND FUTURE RECOMMENDATIONS ..</b>		<b>96</b>
5.1	Conclusions .....	96
5.2	Recommendations for Future Research .....	98
<b>REFERENCES .....</b>		<b>100</b>
<b>LIST OF PUBLICATIONS</b>		

## LIST OF TABLES

		<b>Page</b>
Table 2.1	Relationship between AM and zenith angle.....	8
Table 2.2	Standard potential reduction, $E^0$ of $H_2O_2$ and Ag materials. ....	17
Table 2.3	Electrical properties of b-Si solar cells synthesized by various methods. ....	20
Table 3.1	Parameters for the deposition of Ag thin film using RF sputtering.....	24
Table 4.1	Summary of morphological properties from AFM and FESEM when varying etching time parameter. ....	47
Table 4.2	Potential $J_{sc(max)}$ and potential $J_{sc(max)}$ enhancement of b-Si with various etching times. C-Si wafer is used as a reference. ....	51
Table 4.3	Summary of morphological and optical properties when varying etching time parameter.....	52
Table 4.4	Summary of morphological properties from AFM and FESEM when varying volume ratios of $H_2O$ . ....	55
Table 4.5	Potential $J_{sc(max)}$ and potential $J_{sc(max)}$ enhancement of b-Si etched in different etchant volume ratios. Planar c-Si is used as a reference.....	60
Table 4.6	Summary of morphological and optical properties when etchant ratio of DI $H_2O$ are varied.....	61
Table 4.7	Summary of morphological properties from AFM and FESEM when varying volume ratios of HF and $H_2O_2$ . ....	66
Table 4.8	Potential $J_{sc(max)}$ and potential $J_{sc(max)}$ enhancement of b-Si etched with different volume ratios. Planar c-Si is used as a reference. ....	70
Table 4.9	Summary of morphological and optical properties for the wafers with varying HF and $H_2O_2$ ratios. ....	71
Table 4.10	Summary of morphological properties from AFM and FESEM of b-Si when annealed at different temperature.....	76

Table 4.11	Potential $J_{sc(max)}$ and potential $J_{sc(max)}$ enhancement of b-Si wafers annealed with different temperatures. Planar c-Si is used as a reference.....	81
Table 4.12	Summary of morphology and optical properties when annealing temperatures are varied. ....	82
Table 4.13	Elements detected (in atomic %) on b-Si after etching process (before Ag removal).....	84
Table 4.14	Elements detected (in atomic %) on b-Si after Ag removal.....	84
Table 4.15	Atomic percentage of respective elements found on the surface of b-Si wafer after diffusion process. ....	86
Table 4.16	Potential $J_{sc(max)}$ of b-Si wafers after emitter doping at various temperatures. B-Si before emitter doping is used as a reference.	90
Table 4.17	Summary of sheet resistance, mobility and carrier concentration of $n^+$ emitter layer on b-Si doped at various temperatures.....	90
Table 4.18	Summary from J-V curves for planar c-Si and b-Si solar cells...	94

## LIST OF FIGURES

		<b>Page</b>
Figure 1.1	PV technologies by product types (Wang & Barnett, 2019).....	1
Figure 1.2	Annual solar PV capacity from 2008-2018 (REN21, 2019).....	2
Figure 1.3	Schematic diagram of indirect band gap of c-Si (Yuan et al., 2018). .....	3
Figure 1.4	B-Si solar cell (left: black colour) and conventional c-Si solar cell (right: dark blue colour) (Becky B., 2018).....	4
Figure 2.1	The air mass conditions under different zenith angle (Laser Focus World, 2009). .....	8
Figure 2.2	Standard solar spectrums of AM 1.5G, AM 1.5D and AM 0 (Macksey, 2019). The American Society for Testing and Materials (ASTM) G-173 spectra represents the terrestrial solar spectral irradiance on a surface of specified orientation under only one set of specified atmospheric conditions. ....	9
Figure 2.3	The photon flux of various optical path length in c-Si with different thicknesses (Rand et al., 2002).....	10
Figure 2.4	Optical length of incident lights for planar c-Si (left) and pyramid texture c-Si (right). Note that the schematic diagram is not to scale.....	11
Figure 2.5	Lambertian reflector used at rear surface to enhance light trapping (Honsberg & Bowden, 2010).....	12
Figure 2.6	(a) For b-Si: Gradual change of refractive index from $n=1$ (air) to $n=3.8$ (c-Si). (b) For planar c-Si: Abrupt change of refractive index from $n=1$ (air) to $n=3.8$ (c-Si). ....	13
Figure 2.7	Optical path of incident light in planar c-Si (left) and b-Si (right). Note that the schematic diagram is not to scale. ....	13
Figure 2.8	RIE process in a multi-cathode system (Liu et al., 2014). ....	14
Figure 2.9	Mechanism of nanopores formation during two-step MACE process.....	18
Figure 3.1	Flow chart of detailed procedures for the synthesis of b-Si.....	22

Figure 3.2	(a) Auto HHV 500 Sputtering Coater (b) Chamber of sputtering where the c-Si wafers are loaded. ....	24
Figure 3.3	(a) Blue furnace for annealing process and (b) schematic configuration for thermal annealing. ....	25
Figure 3.4	Etching setup to form b-Si. ....	26
Figure 3.5	Schematic illustration of Si nanopores formed by MACE method. ....	27
Figure 3.6	(a) AFM (Model:Dimension EDGE, BRUKER) used to scan the topography of b-Si wafers. (b) Principle of AFM operation (Deng et al., 2018). ....	29
Figure 3.7	(a) FESEM FEI Nova NanoSEM 450. (b) Schematic diagram of basic working principle of FESEM (Jusman et al., 2014). ....	30
Figure 3.8	UV-Vis-NIR spectrophotometer used to measure reflection and transmission of a sample. ....	31
Figure 3.9	Schematic of diffuse and specular reflections (Honsberg & Bowden, 2010). ....	32
Figure 3.10	Flow chart for processing of homojunction b-Si solar cell. ....	33
Figure 3.11	(a) Spin coater (Model:SCS G3P-8) (b) Hot plate used to harden the coating on the wafer. ....	34
Figure 3.12	Grey furnace used to drive-in phosphorus via diffusion process. ....	35
Figure 3.13	(a) Thermal evaporator used to deposit Ag and Al as front and rear contacts respectively and (b) schematic diagram of thermal evaporator. ....	36
Figure 3.14	The design of metal mask for evaporation of Ag contact on b-Si wafer. ....	36
Figure 3.15	(a) The metal mask and (b) the b-Si after being deposited with Ag contact. ....	37
Figure 3.16	Hall effect measurement system (Model: Lakeshore Controller 601/DRC-93CA). ....	38
Figure 3.17	Solar simulator that is used for I-V measurement of solar cells. ....	40
Figure 3.18	The comparison of white LED and AM 1.5G solar simulator spectra (Llenas & Carreras, 2019). ....	40
Figure 3.19	The schematic figure of I-V characteristic of a solar cell. ....	41

Figure 4.1	Images of c-Si wafers after being etched with various etching times. (a) c-Si reference (b) after 35 s (c) after 70 s (d) after 90 s (e) after 120 s and (f) after 180 s.....	43
Figure 4.2	AFM images of different b-Si nanotextures after etched with etching times of (a) 35 s, (b) 70 s, (c) 90 s, (d) 120 s and (e) 180 s. ....	44
Figure 4.3	FESEM images of c-Si (a) after sputtered with 15 nm Ag film and (b) after annealed in N <sub>2</sub> atmosphere at 230°C temperature for 40 min. ....	45
Figure 4.4	Top view FESEM images of b-Si nanopores after being etched for (a) 35 s, (b) 70 s, (c) 90 s, (d) 120 s and (e) 180 s.....	46
Figure 4.5	(a) Reflection and (b) absorption profiles of b-Si wafers after being etched at different durations. Planar c-Si is used as a reference.....	48
Figure 4.6	Reflection and absorption curves of wafers at 600 nm wavelength. ....	48
Figure 4.7	Relationship between average interpore distance (in b-Si) and reflection (at wavelength of 600 nm). Noted that the reflection of 3%, 7%, 8%, 9% and 10% are belongs to 70 s, 35 s, 90 s, 120 s and 180 s. ....	49
Figure 4.8	Measured interpore distance between one centre to the adjacent centre nanopores of b-Si wafer etched at (a) 35 s, (b) 70 s, (c) 90 s, (d) 12 s and (e) 180 s. ....	50
Figure 4.9	Images of (a) c-Si reference wafer and b-Si wafers etched in different volume ratios of (b) 1:5:5 (c) 1:5:10 and (d) 1:5:20.....	53
Figure 4.10	AFM images of b-Si nanotextures with different etchant volume ratios; (a) 1:5:5 (b) 1:5:10 (c) 1:5:20. ....	54
Figure 4.11	FESEM images of b-Si wafers synthesized by varying the etchant volume ratios; (a) 1:5:5 (b) 1:5:10 and (c) 1:5:20.....	55
Figure 4.12	(a) Reflection and (b) absorption profiles for b-Si etched with different volume ratios. Planar c-Si is used as a reference. ....	57
Figure 4.13	Reflection and absorption for b-Si at wavelength of 600 nm with different etchant volume ratios.....	57

Figure 4.14	Relationship between average interpore distance (in b-Si) and reflection (at wavelength of 600 nm). Noted that the reflection of 3%, 6% and 12% are belongs to 1:5:10, 1:5:20 and 1:5:10 volume ratios respectively.....	58
Figure 4.15	The measurement of the interpore distance for all b-Si wafers etched in volume ratio of (a) 1:5:5, (b) 1:5:10 and (c) 1:5:20.....	59
Figure 4.16	Images of (a) c-Si wafer as reference and b-Si wafers etched with different volume ratios of (b) 1:5:10, (c) 2:4:10, (d) 3:3:10, (e) 4:2:10 and (f) 5:1:10.....	62
Figure 4.17	AFM images of b-Si wafers after being etched in different etchant volume ratios (a) 1:5:10, (b) 2:4:10, (c) 3:3:10, (d) 4:2:10 and (e) 5:1:10. ....	63
Figure 4.18	Top view FESEM images for b-Si wafers etched with different etchant volume ratios (a) 1:5:10, (b) 2:4:10, (c) 3:3:10, (d) 4:2:10 and (e) 4:1:10. ....	65
Figure 4.19	Illustration for MACE process. $H_2O_2$ act as oxidizing agent undergoes reduction reaction where catalyzed by Ag metal because $H_2O_2$ standard potential reduction is higher about 1.76 V compared to $Ag^+$ (0.80 V) (Li et al., 2020).....	66
Figure 4.20	(a) Reflection and (b) absorption profiles of b-Si etched in different volume ratios of HF and $H_2O_2$ . Planar c-Si is used as a reference.....	67
Figure 4.21	Reflection (primary axis) and absorption (secondary axis) of b-Si wafers at wavelength of 600 nm with different etchant volume ratios.....	68
Figure 4.22	Relationship between average interpore distance (in b-Si) and reflection (at wavelength of 600 nm) for b-Si wafers etched with different etchant volume ratios. Noted that the reflection of 3%, 11%, 15%, 19% and 30% are belongs to 1:5:10, 2:4:10, 3:3:10, 4:2:10 and 5:1:10 volume ratios respectively. ....	69
Figure 4.23	The measurement of the interpore distance for all b-Si wafers etched in volume ratio of (a) 1:5:10, (b) 2:4:10, (c) 3:3:10, (d) 4:2:10 and (e) 5:1:10. ....	70

Figure 4.24	The images of (a) c-Si reference wafer and b-Si wafers annealed at different temperatures; (b) 200°C, (c) 230°C and (d) 260°C..	72
Figure 4.25	AFM images of b-Si wafers annealed at different temperatures; (b) 200°C, (c) 230°C and (d) 260°C. ....	73
Figure 4.26	Top view FESEM images of Ag NPs after being annealed at different temperatures; (a) 200°C, (b) 230°C and (c) 260°C. ....	74
Figure 4.27	Top view FESEM images of b-Si after etching process. The wafers are annealed at different temperatures; (a) 200°C, (b) 230°C and (c) 260°C. ....	76
Figure 4.28	(a) Reflection and (b) absorption profiles of b-Si with different annealing temperatures. Planar c-Si is used as a reference. ....	77
Figure 4.29	Reflection (primary axis) and absorption (secondary axis) at wavelength 600 nm of c-Si and b-Si wafers that have been annealed with different annealing temperatures. ....	78
Figure 4.30	Relationship between average interparticle and interpore distance (in b-Si) and corresponding reflection (at wavelength of 600 nm) for b-Si wafers annealed with different annealing temperatures. Noted that the interparticle distance and nanopores distance with reflection of 3%, 7% and 13% are belongs to different annealing temperatures of 230°C, 200°C and 260°C respectively. ....	79
Figure 4.31	The measurement of the interparticle distance for the wafers with annealing temperature of (a) 200°C, (b) 230°C and (c) 260°C. ....	80
Figure 4.32	Measured interpore distance for the b-Si annealed at temperature of (a) 200°C, (b) 230°C and (c) 260°C. ....	80
Figure 4.33	Cross-sectional FESEM image of optimized b-Si wafer which produces the lowest broadband reflection within the 300-1100 nm wavelength region. ....	83
Figure 4.34	EDX analysis of Ag NPs on b-Si surface (a) before removal (b) after removal through sonication. ....	84
Figure 4.35	EDX analysis of b-Si wafer after diffusion process. ....	86
Figure 4.36	Top view and cross-sectional FESEM images of b-Si doped with phosphorus at different doping temperatures (a) (b) 850°C, (c) (d) 900°C and (e) (f) 950°C. ....	87

Figure 4.37	(a) Reflection and (b) absorption profiles of b-Si after emitter doping process at various temperatures. B-Si before emitter doping is used as a reference.....	88
Figure 4.38	Reflection and absorption of b-Si at 600 nm before and after emitter doping at various temperatures. B-Si before emitter doping is used as a reference.....	89
Figure 4.39	Schematic diagram of complete c-Si and b-Si solar cell.....	91
Figure 4.40	J-V curves of planar c-Si solar cell (as reference) and b-Si solar as measured by RGB LED illumination system. ....	93
Figure 4.41	Top view of c-Si after doping process. Same wafer is tested at two different locations and it is observed that some areas of the wafer have needle-like texture and some areas have flat textures.....	95

## LIST OF SYMBOLS

A	Absorption
$J_{sc}$	Short-circuit current density
$J_{sc(max)}$	Maximum short-circuit current density
n	Refractive index
R	Reflection
$R_s$	Sheet resistivity
$R_{sh}$	Shunt resistance
T	Transmission
$V_{oc}$	Open-circuit voltage
$\lambda$	Wavelength

## LIST OF ABBREVIATIONS

AFM	Atomic Force Microscopy
Ag	Silver
AgNO <sub>3</sub>	Silver nitrate
Al	Aluminium
Ar	Argon
ARC	Anti-reflecting coating
ASTM	American Society for Testing and Materials
Au	Gold
b-Si	Black silicon
BSF	Back surface field
C-Si	Crystalline silicon
CHF <sub>3</sub>	Fluoroform
Cl <sub>2</sub>	Chlorine
C <sub>4</sub> F <sub>8</sub>	Octafluorocyclobutane
Cu	Copper
EQE	External Quantum Efficiency
DI H <sub>2</sub> O	Deionized water
DRIE	Deep Reactive Ion Etching
C <sub>2</sub> H <sub>5</sub> OH	Ethanol
FESEM	Field Emission Scanning Electron Microscopy
HCl	Hydrochloric acid
HF	Hydrofluoric acid
H <sub>2</sub> O <sub>2</sub>	Hydrogen peroxide
H <sub>2</sub> SiF <sub>6</sub>	Hexafluorosilicic acid
IQE	Internal Quantum Efficiency
K <sub>2</sub> Cr <sub>2</sub> O <sub>7</sub>	Potassium dichromate
KMnO <sub>4</sub>	Potassium permanganate
MACE	Metal-Assisted Chemical Etching
N <sub>2</sub>	Nitrogen
Na <sub>2</sub> S <sub>2</sub> O <sub>8</sub>	Sodium persulfate
Ni	Nickel

O <sub>2</sub>	Oxygen
PIII	Plasma Immersion Ion Implantation
PSG	Phosphosilicate glass
Pt	Platinum
PV	Photovoltaic
P <sub>2</sub> O <sub>5</sub>	Phosphorus pentoxide
RCA	Radio Corporation of America
RIE	Reactive Ion Etching
RF	Radio frequency
RGB	Red Green Blue
SiCl <sub>4</sub>	Silicon tetrachloride
SF <sub>6</sub>	Sulphur hexafluoride
SiF <sub>6</sub>	Silicon hexafluoride
Si <sub>3</sub> N <sub>4</sub>	Silicon nitride
SiO <sub>2</sub>	Silicon dioxide
SPM	Scanning Probe Microscopy
STC	Standard Test Conditions
WAR	Weighted average reflection

# SINTESIS DAN PENCIRIAN SILIKON HITAM BERBANTUKAN PUNARAN KIMIA PERAK UNTUK SEL SURIA

## ABSTRAK

Silikon kristal (c-Si) mempunyai penyerapan cahaya yang kurang baik kerana sifat jurang jalur tak langsung dan refleksi tinggi dari permukaannya (kira-kira 35% dalam kawasan cahaya nampak). Masalah ini dapat diselesaikan dengan mentekstur permukaan wafer c-Si untuk mengurangkan pantulan jalur lebarnya. Silikon hitam (b-Si) atau c-Si tekstur nano, mempunyai potensi besar untuk aplikasi dalam sel solar kerana penyerapan cahaya dalam jalur lebar yang unggul dalam kawasan panjang gelombang 300-1100 nm. Dalam kajian ini, punaran kimia yang berbantuan logam (MACE) dua-langkah digunakan untuk mensintesis b-Si dengan menggabungkan penyepuhlindapan bersuhu rendah untuk filem perak (Ag) dan punaran jangka pendek untuk wafer c-Si. Untuk fabrikasi b-Si, wafer jenis-p (100) c-Si didepositkan dengan 15 nm filem Ag menggunakan proses percikan frekuensi radio (RF). Kemudian, wafer melalui proses penyepuhlindapan pada suhu rendah (230-260°C) di dalam ambien nitrogen (N<sub>2</sub>), yang menghasilkan nanopartikel (NPs) Ag. Seterusnya, wafer c-Si dipunarkan di dalam larutan asid hidrofluorik: hidrogen peroksida: air ternyahion (HF:H<sub>2</sub>O<sub>2</sub>:DI H<sub>2</sub>O) untuk jangka masa 35-180 s. Kesan masa punaran, nisbah isipadu bahan punaran dan suhu penyepuhlindapan ke atas sifat permukaan morfologi dan optik dengan menggunakan AFM, FESEM dan UV-Vis-NIR (di antara panjang gelombang 300-1100 nm) telah dikaji. Daripada kajian ini, b-Si yang mempunyai pantulan jalur lebar yang paling rendah dihasilkan daripada penyepulindapan pada suhu 230°C selama 40 min dan punaran dalam larutan HF:H<sub>2</sub>O<sub>2</sub>: DI H<sub>2</sub>O (isipadu 1:5:10) selama 70 s. Pantulan terendah daripada wafer b-Si bernilai 3% pada panjang

gelombang 600 nm dengan pantulan purata wajaran (WAR=8%). B-Si ini mempunyai kelebaran purata 50-100 nm dan ketinggian purata 300-400 nm untuk nanotekstur yang terhasil. Untuk fabrikasi sel suria, asid fosforik ( $H_3PO_3$ ) dan 2-butanol diresap ke dalam wafer b-Si menggunakan suhu 850-950°C selama 20 min untuk membentuk pemancar  $n^+$  pada bahagian hadapan. Ag dan Aluminium (Al) disejat secara terma di depan dan belakang wafer masing-masing untuk membentuk sentuhan elektrik. Dari pengukuran arus-voltan, sel solar b-Si menunjukkan arus litar pintas ( $J_{sc}$ ) 20 mA/cm<sup>2</sup>, voltan litar terbuka ( $V_{oc}$ ) 423 mV dan faktor isi (FF) 25.4%. Ini mewakili kecekapan penukaran 5.2%. Sebaliknya, sel solar c-Si rujukan berpermukaan rata menunjukkan  $J_{sc}$  7 mA/cm<sup>2</sup>,  $V_{oc}$  390 mV dan FF 21.7%. Penyebab utama kecekapan penukaran yang rendah untuk sel solar dipercayai disebabkan oleh kehilangan teduhan yang tinggi dan pembentukan simpang p-n yang berkualiti rendah.

# SYNTHESIS AND CHARACTERIZATION OF BLACK SILICON BY SILVER-ASSISTED CHEMICAL ETCHING FOR SOLAR CELL

## ABSTRACT

Crystalline silicon (c-Si) suffers from poor light absorption due to its indirect band gap and high reflection from its surface (about 35% in the visible region). This problem can be solved by texturing the surface of c-Si wafer to reduce its broadband reflection. Black silicon (b-Si) or nanotextured c-Si, has a huge potential for applications in solar cell due to its superior broadband light absorption within 300-1100 nm wavelength region. In this work, two-step metal-assisted chemical etching (MACE) is used to synthesize b-Si by combining low-annealing temperature of silver (Ag) film and short duration of etching of the c-Si wafer. For the b-Si fabrication, p-type (100) c-Si wafers are deposited with 15 nm Ag film using radio frequency (RF) sputtering process. Subsequently, the Ag film is annealed at low temperatures (200-230°C) for 40 min in nitrogen (N<sub>2</sub>) ambient, producing Ag nanoparticles (NPs). Then, the c-Si wafers with the Ag NPs are etched in a solution containing hydrofluoric acid:hydrogen peroxide:deionized water (HF:H<sub>2</sub>O<sub>2</sub>:DI H<sub>2</sub>O) for a short duration (35-180 s). Effects of etching time, etchant volume ratio and annealing temperature towards surface morphological and optical properties by using atomic force microscope (AFM), field emission scanning electron microscope (FESEM) and UV-Vis-NIR (within 300-1100 nm wavelength region) of b-Si are then investigated. From the investigation, the b-Si with the lowest broadband reflection is produced by annealing at 230°C for 40 min and etched for 70 s using HF:H<sub>2</sub>O<sub>2</sub>:DI H<sub>2</sub>O (1:5:10 by volume). The lowest reflection of the b-Si wafer is 3% at wavelength of 600 nm, with

weighted average reflection (WAR) of 8%. The b-Si demonstrates average width and height of about 50-100 nm and 300-400 nm respectively for the nanotextures.

For solar cell fabrication, the b-Si is diffused with phosphoric acid ( $\text{H}_3\text{PO}_4$ ) and 2-butanol using temperatures between 850 to 950°C for 20 min to form front  $\text{n}^+$  emitter. The emitter is characterized using Hall effect measurement. Ag and aluminium (Al) are thermally evaporated on the front and rear surfaces respectively to form electrical contacts. From current-voltage measurement, the b-Si solar cells demonstrate short-circuit current density ( $J_{\text{sc}}$ ) of 20  $\text{mA}/\text{cm}^2$ , open-circuit voltage ( $V_{\text{oc}}$ ) of 423 mV and fill factor (FF) of 25.4%. This corresponds to conversion efficiency ( $\eta$ ) of 5.2%. On the other hand, the planar c-Si reference solar cells exhibit  $J_{\text{sc}}$  of 7  $\text{mA}/\text{cm}^2$ ,  $V_{\text{oc}}$  of 390 mV and FF of 21.7%. The low conversion efficiency of the solar cells is contributed by high shading loss due to the front metal fingers and poor quality of p-n junction formation.

# CHAPTER 1

## INTRODUCTION

### 1.1 Background

Crystalline silicon (c-Si) solar cell dominates more than 90% of photovoltaic (PV) market (Burger, 2017; Chen et al., 2019; Löper et al., 2015). This is because the c-Si solar cell is a mature technology and exhibits high conversion efficiency. To date, monocrystalline silicons (mono c-Si) solar cells with efficiency up to 25% has been demonstrated by (Li et al., 2020). Figure 1.1 shows different types of PV technologies available in the PV market. From 107 GW of overall PV installation in 2018, about 97% (about 104 GW) is based on c-Si solar cells (based on p-type and n-type c-Si cells). The economies of scale of the c-Si solar cells leads to reducing technology cost (US\$/Watt<sub>p</sub>) (Jäger-Waldau, 2019; Powell et al., 2015). In the recent five years, the technology cost for c-Si solar cells has dropped by more than 70%, to below US\$0.30/Watt<sub>p</sub>.

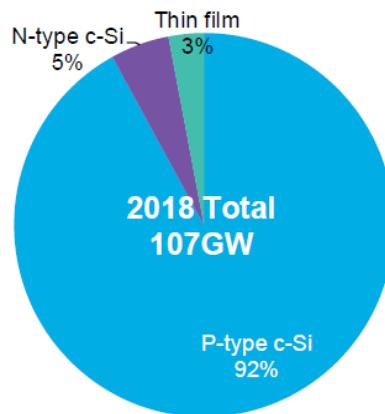


Figure 1.1 PV technologies by product types (Wang & Barnett, 2019).

Figure 1.2 illustrates annual solar PV capacity from 2008 to 2018. The figure shows the cumulative capacity of global market for solar PV increased from 15 GW in 2008 to 505 GW in 2018. The China dominates the annual installation of PV system.

The China PV market stabilized in 2014 and grew until 2018 which has made China as a country that leading the cumulative capacity followed by United State, Japan German and India. The China also continued to dominated the global solar PV manufacturing in industry. The best top three solar PV manufacturing companies has conquered by China-based companies: (i) Jinko Solar, (ii) JA Solar and (iii) Trina Solar. These companies are extensively exploring on Passivated Emitter Rear Cell (PERC) technology as it increases efficiencies with modest investment.

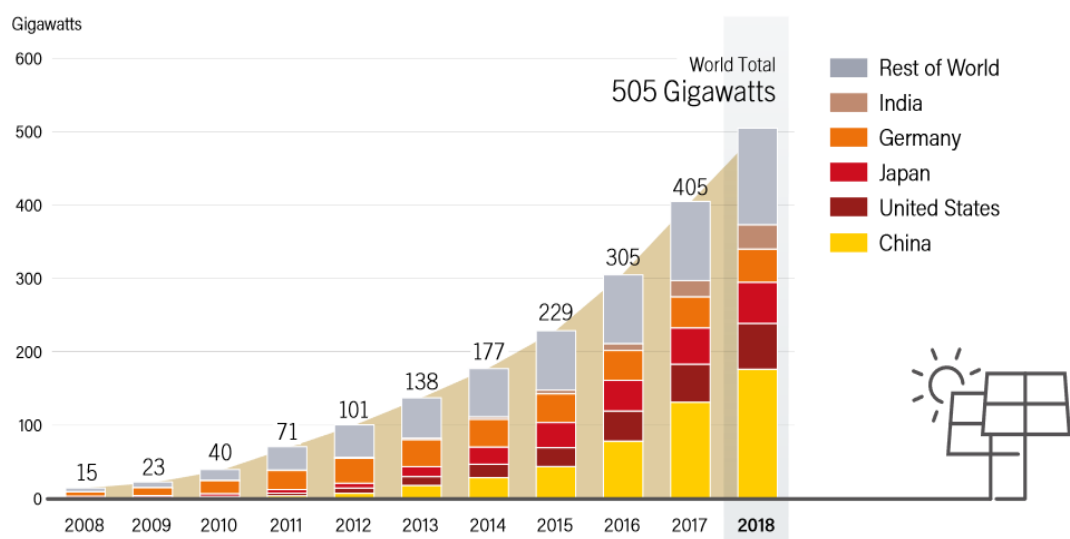


Figure 1.2 Annual solar PV capacity from 2008-2018 (REN21, 2019).

## 1.2 Problem statement

Despite the domination of c-Si in the PV market, it is known that c-Si is a poor light absorber. This is because c-Si is an indirect band gap semiconductor material. This means that the maximum of valence band (VB) and the minimum of conduction band (CB) in c-Si does not lie at the same value of electron crystal momentum,  $k$ , as depicted in Figure 1.3. To enable electron transition from the VB to CB during light absorption by the c-Si, extra phonon needs to be involved. This causes the c-Si to exhibit poor light absorption. Furthermore, c-Si also suffers from high surface

reflection. As light is incident on the surface of c-Si, about 35% of the light is reflected. This is due to the change of refractive index ( $n$ ) experienced by the light (photons) as it travels from air ( $n=1.0$ ) to c-Si ( $n=3.8$ ) in the visible region. The abrupt change of refractive index leads to high Fresnel reflection from the c-Si surface. The 35% reflection translates into a high optical loss in the c-Si solar cell (Deraoui et al., 2013). High optical losses results in low photocurrent from the solar cell.

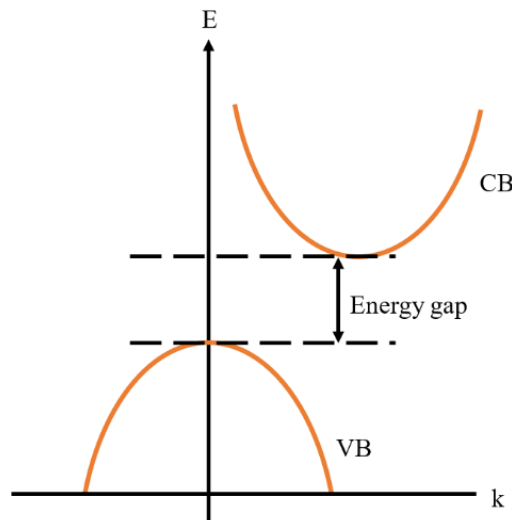


Figure 1.3 Schematic diagram of indirect band gap of c-Si (Yuan et al., 2018).

To ensure superior light absorption in c-Si solar cell, a surface modification of c-Si is required. B-Si is a technology in which surface modification leads to formation of nanotextures on the c-Si wafer surface. The nanotextures are produced on the c-Si surface via etching process (Otto et al., 2015; Wendisch et al., 2020). The b-Si reduces broadband reflection of c-Si from 35% (for planar c-Si) to below 5% in 300-1100 nm wavelength region (Algasinger et al., 2013). The suppressed broadband reflection leads to high absorption. The superior broadband light absorption makes the b-Si appears black to the naked eyes. This is in comparison to the typical dark blue appearance of the conventional c-Si solar cells which have front pyramids textures

coated with a thin anti-reflective coating (ARC). The comparison of the b-Si and conventional c-Si solar cells is illustrated in Figure 1.4.



Figure 1.4 B-Si solar cell (left: black colour) and conventional c-Si solar cell (right: dark blue colour) (Becky B., 2018).

According to Chartier et al., 2008, the b-Si is formed when Ag NPs are deposited on c-Si by electroless metallization, where c-Si is dipped in a solution of HF (0.14M) and  $\text{AgNO}_3$  ( $5 \times 10^{-4}\text{M}$ ) for 1-5 min at  $180^\circ\text{C}$ . After the desired Ag NPs are formed, the sample was etched in solutions of HF (40%),  $\text{H}_2\text{O}_2$  (35%) and DI  $\text{H}_2\text{O}$  ( $18.2 \text{ M}\Omega \text{ cm}$ ) to form b-Si (Chartier et al., 2008). In 2013, Liu et al. has fabricated b-Si using two-step metal-assisted chemical etching (MACE) method by evaporating 8-30 nm of Ag film on n-type c-Si wafer followed by annealing for 10 min at low temperature ( $150\text{-}300^\circ\text{C}$ ). Then, the wafer was etched in HF and  $\text{H}_2\text{O}_2$  for a long time between 5-20 min. In this work, only surface morphological results were reported. In this work, nanowires with lengths in the range of 0.5 to  $2 \mu\text{m}$  were formed (Liu et al., 2013).

A recent study on MACE process to form b-Si has been conducted by (Wu et al., 2016). In this work, an Ag film with 80 nm thickness was deposited on p-type c-Si wafers by magnetron sputtering. Subsequently, the wafers were annealed at high

temperature (300-800°C) for a long time (60 min). Then, the wafers were etched in solution containing HF (40%) and H<sub>2</sub>O<sub>2</sub> (30%) for 30 min at 50°C. The lowest weighted average reflection (WAR) obtained was 4.7% when the annealing was conducted at 600°C.

The motivation of this research is to explore a simple synthesis method to fabricate b-Si for solar cell application using p-type (100) wafer and utilize low annealing temperature (under 300°C) and short etching duration (under 200 s). In this work, b-Si will be produced by a two-step MACE process. This process involves deposition of Ag film of 15 nm thickness on c-Si wafer, followed by annealing at low temperature for a short duration, as mentioned above. The optimized b-Si will then be used to fabricate solar cell.

### **1.3 Objectives**

The objectives of this work are as the following:

1. To synthesize p-type b-Si by two-step metal-assisted chemical etching (MACE) process.
2. To investigate surface morphological, optical and electrical properties of b-Si as an active layer for solar cell.
3. To evaluate and compare the performance of b-Si solar cells in comparison to planar c-Si solar cells.

### **1.4 Thesis outlines**

This section briefly explains the flow of this thesis. There are five chapters in this thesis and all the contents of each chapter are outlined as below.

Chapter 1 outlines the introduction to research, motivation behind the work followed by research objectives of this thesis.

Chapter 2 presents the theory of solar radiation, c-Si, light trapping and formation of b-Si. This chapter also includes the b-Si fabrication method and the mechanism behind the two-step MACE process that has been employed in this research.

Chapter 3 discusses the methodology to synthesize b-Si and to fabricate b-Si solar cells. Surface morphological, optical and electrical characterizations of b-Si and b-Si solar cells are also explained in this chapter.

Chapter 4 presents the results obtained from this work. This covers the properties of b-Si until the performance of b-Si solar cells. The results are also discussed with relation to theory and previous findings in the literature.

Chapter 5 concludes the findings from this research. At the end of this chapter, a few recommendations are outlined for future works. The aim is to improve the performance of b-Si solar cells synthesised by MACE process.

## CHAPTER 2

### LITERATURE REVIEW

#### 2.1 Introduction

In this chapter, the background related to this work is discussed. The background includes solar radiation and light trapping in c-Si solar cell. This chapter also describes how b-Si is fabricated and the mechanism involved during two-step MACE process.

#### 2.2 Solar radiation

Solar radiation is an electromagnetic radiation emitted by the Sun which consists of photons of different energies (i.e. different wavelengths). The photon energy (E) can be expressed using equation:

$$E = h\nu = \frac{hc}{\lambda} \quad (2.1)$$

where E is photon energy, h is a plank constant ( $6.626 \times 10^{-34}$  J/s or  $3.13 \times 10^{-15}$  eV/s),  $\nu$  is the frequency of light (Hz), c is speed of light ( $2.99 \times 10^8$  m/s) and  $\lambda$  is the wavelength of light (m). The solar spectrum is also called as solar energy irradiation ( $\text{W}/\text{m}^2\text{nm}^{-1}$ ) which ranges from ultraviolet, visible and infrared regions.

The pathlength of the sunlight to reach the earth surface is called as Air Mass (AM). The AM can be calculated by the following equation:

$$AM = \frac{1}{\cos \theta} \quad (2.2)$$

where AM is air mass and  $\theta$  is a zenith angle (vertical) in degree between the sun and the point overhead. In Table 2.1, the relationship between the air mass and zenith angle is illustrated. It is shown that when increasing the zenith angle, the air mass will increase too. This solar energy distribution just outside the Earth's atmosphere is referred as AM 0 because no air is measured between the Sun and the receiver. An AM 1 is referred to the sunlight strikes directly over head and gone through the air at  $0^\circ$  zenith angle as

shown in Figure 2.1. A standard spectrum at the Earth surface is either AM 1.5G (G is global, which includes direct and diffuse radiations) or AM 1.5D (includes direct radiation only). The radiation of AM 1.5G is 10% higher than AM 1.5D. The radiant power density of a AM 1.5G is 1 kW/m<sup>2</sup> at 25°C. The radiant power density of these radiations varies with wavelength as depicted in Figure 2.2.

Table 2.1 Relationship between AM and zenith angle.

Air mass (AM)	Zenith angle ( $\theta$ )
AM 0	-
AM 1	0
AM 1.5	48.2°

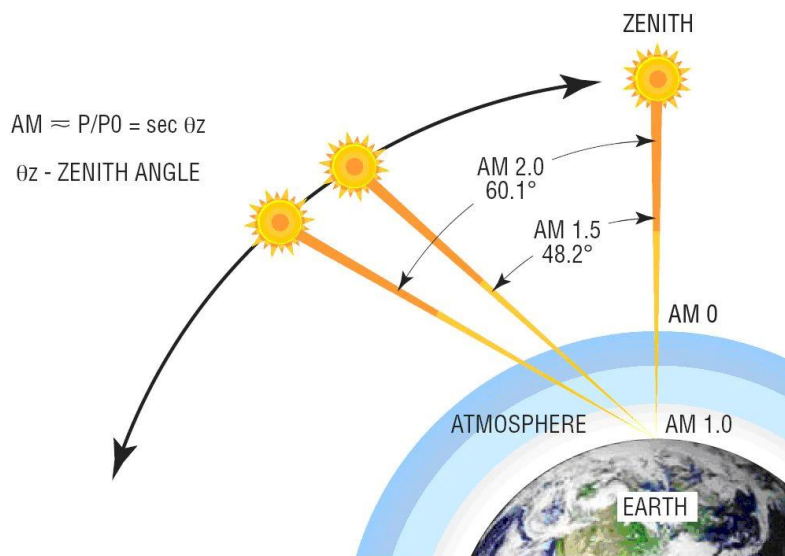


Figure 2.1 The air mass conditions under different zenith angle (Laser Focus World, 2009).

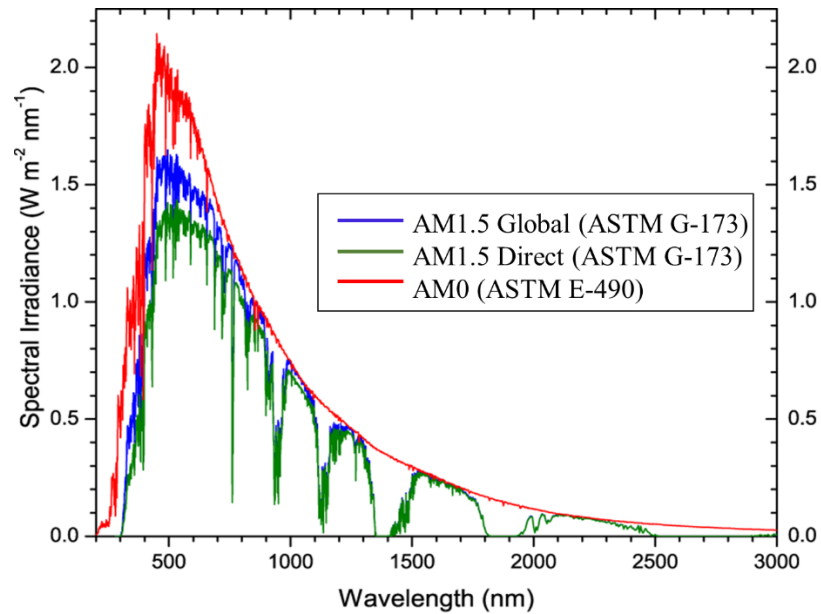


Figure 2.2 Standard solar spectrums of AM 1.5G, AM 1.5D and AM 0 (Macksey, 2019). The American Society for Testing and Materials (ASTM) G-173 spectra represents the terrestrial solar spectral irradiance on a surface of specified orientation under only one set of specified atmospheric conditions.

### 2.3 Light trapping

Light trapping is a strategy to trap incident light (photons) in solar cell. The ultimate goal of light trapping is to maximize light absorption in the solar cell (Kordrostami & Yadollahi, 2020). Maximized absorption leads to high photocurrent in the solar cell. As previously mentioned, c-Si has poor light absorption. This owes to its low absorption coefficient within the wavelength of interest (UV, visible and infra-red regions) for PV conversion process. This is due to its indirect band gap nature. The amount of light that is absorbed in a c-Si based solar cell depends on its absorption coefficient and optical path length within the active layer. Thin c-Si (e.g 1  $\mu\text{m}$ ) absorbs only a fraction of the incident photons. Most of the incident photons from the visible and IR regions are not absorbed. On the other hand, thick c-Si (e.g 200  $\mu\text{m}$ ) absorbs a greater fraction of the incident photons, particularly in the long wavelength region (i.e. IR region onwards). This is illustrated in Figure 2 which shows that as the c-Si thickness

increases, more incident photons particularly from the long wavelength region will be absorbed in the c-Si. For a complete absorption of the incident spectrum, a very thick c-Si (above 500  $\mu\text{m}$ ) is needed. This will not be economical to enable c-Si solar cell technology with low technology cost (US\$/Watt<sub>p</sub>) in the market (Basuet et al., 2015; Jia et al., 2018).

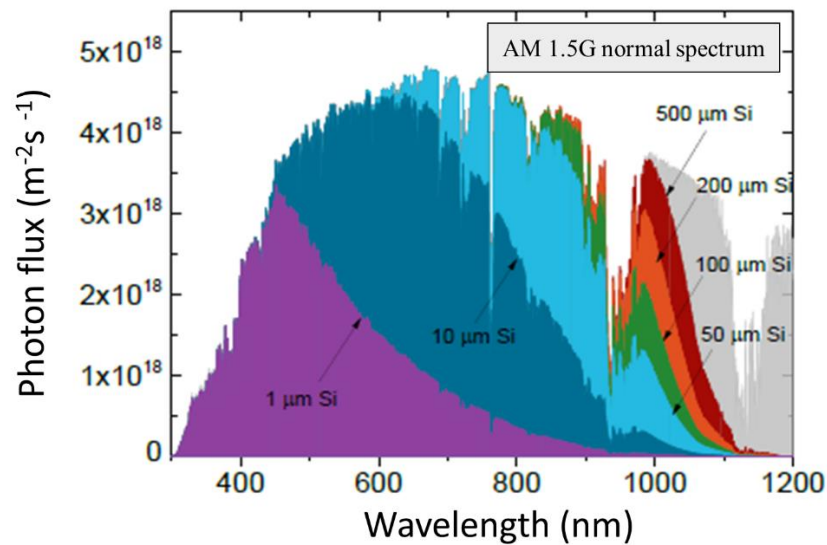


Figure 2.3 The photon flux of various optical path length in c-Si with different thicknesses (Rand et al., 2002).

To overcome this issue, texturing of front, rear or both sides of the c-Si wafer is inevitable. Texturing these surfaces forces the incoming light to bounce more than once within the solar cell. This results in multiple rays of light to enter and take a longer path through the c-Si wafer. This phenomena is called light trapping (Manzoor et al., 2020). In industrial monocrystalline silicon (mono c-Si) solar cells, texturing is carried out by etching c-Si wafers in potassium hydroxide (KOH) or sodium hydroxide (NaOH) solution at 80°C for several minutes (Mahmoud Al & Lahlouh, 2017). This texturing produces microscale random upright pyramids on the wafer surface. The pyramids are used to scatter the incident light into multiple angles. Then, the rays which enter the c-Si experience multiple bounces due to multiple total internal reflection (Wang & Qi,

2019). This leads to light trapping in the c-Si absorber. This reduces broadband reflection (within 300-1100 nm wavelength region) from 35% for planar c-Si to around 11-15% for c-Si with front pyramid textures (Han et al., 2013; Prajapati et al., 2012). Due to the suppressed broadband reflection, light absorption is increased. This phenomenon is shown in Figure 2.4 below.

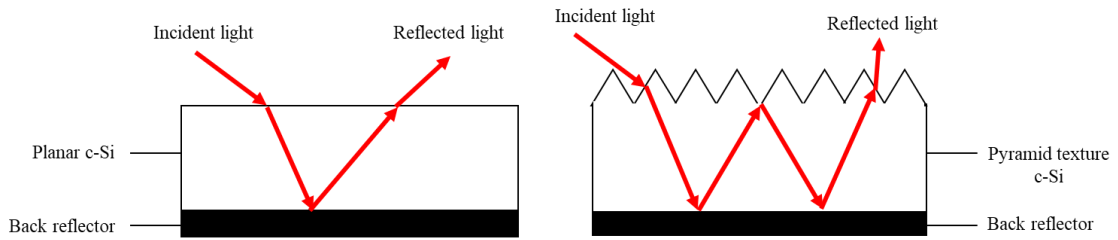


Figure 2.4 Optical length of incident lights for planar c-Si (left) and pyramid texture c-Si (right). Note that the schematic diagram is not to scale.

Apart from the front pyramid textures, industrial mono c-Si solar cells also utilize a 75 nm-thick silicon nitride ( $\text{SiN}_x$ ) anti-reflective coating (ARC) (with  $n \sim 2.0$ ), which is deposited on top of the pyramid textures by plasma enhanced chemical vapour deposition (PECVD) process. The purpose of the ARC is to further suppress the broadband reflection to below 5% via quarter-wavelength destructive interference effect (Wang et al., 2015). This leads to improved light coupling into the c-Si absorber. However, the ARC can only reduce the reflection at a specific wavelength instead of the whole spectrum. The selected wavelength is designed to be around 600 nm since it represents the peak of the AM 1.5G solar spectrum (Zhou et al., 2017). The further suppression of the reflection results in enhanced light absorption in the c-Si absorber.

In 1982, ‘Yabnovitch Limit’ or ‘Lambertian Limit’ was proposed by Eli Yabnovitch and George D. Cody to solve the limit of light trapping in semiconductor by calculating optical path length enhancement ( $Z$ ) using  $4n^2$ , where  $n$  is the refractive index of a semiconductor (Yablonovitch & Cody, 1982). The ‘Lambertian limit’ can be

achieved by texturing the semiconductor surface so that it mimicks a Lambertian surface. Figure 2.5 shows an example of a Lambertian surface which acts as a back reflector. The Lambertian surface randomizes the reflected light in all directions and consequently results in luminance at same the rate in all directions. The light is reflected in the direction of the rear surface again after it hits the front surface with an angle larger than the critical angle for Si-air interface (which is  $48.6^\circ$ ), thus enhances the optical path length in the solar cell. The Lambertian surface increases the light absorption in the c-Si. However, when the incident light is reflected at an angle less than the critical angle, the light will escape (within this “escape cone”) the c-Si since the apex angle is less than the critical angle.

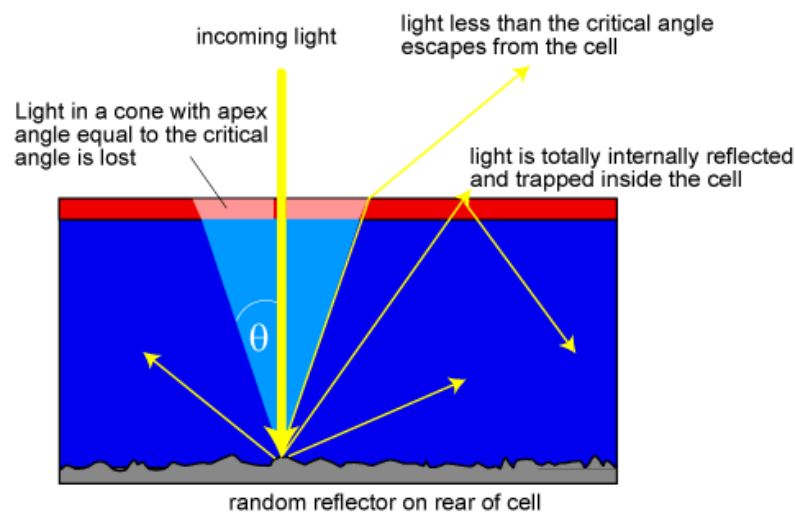


Figure 2.5 Lambertian reflector used at rear surface to enhance light trapping (Honsberg & Bowden, 2010).

## 2.4 Black silicon

Black silicon (b-Si) is a textured surface of c-Si, where the surface is covered by a layer of nanostructures (Hsu et al., 2019). The nanotextures usually have dimension smaller than the wavelength of the incident light. Since the nanotextures have dimension smaller than the wavelength of the light, the light experiences a gradual change of

refractive index from  $n=1$  (air) to  $n=3.8$  (c-Si) at 600 nm as illustrated in Figure 2.6 (a) (Saini & Nair, 2019). This results in improved light coupling into the c-Si and increased absorption. On the contrary, the incident light experiences an abrupt change in refractive index from  $n=1$  (air) to  $n=3.8$  (c-Si) upon striking on the surface of a planar c-Si (Figure 2.6 (b)).

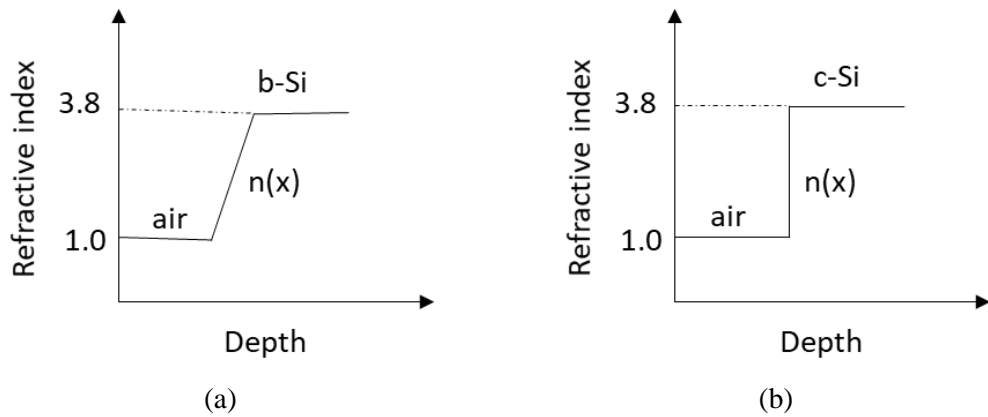


Figure 2.6 (a) For b-Si: Gradual change of refractive index from  $n=1$  (air) to  $n=3.8$  (c-Si). (b) For planar c-Si: Abrupt change of refractive index from  $n=1$  (air) to  $n=3.8$  (c-Si).

Due to the textured surface on b-Si, the optical path length of the light increases in the b-Si as depicted in Figure 2.7. Owing to this feature, b-Si has been widely investigated for applications in photodiodes (Li et al., 2018), photodetectors (Juntunen et al., 2016), biosensors (Cheng & Guan, 2017), lithium ion batteries (Ge et al., 2013), drug deliveries (Abramova et al., 2018) and solar cells (Zhou et al., 2017).

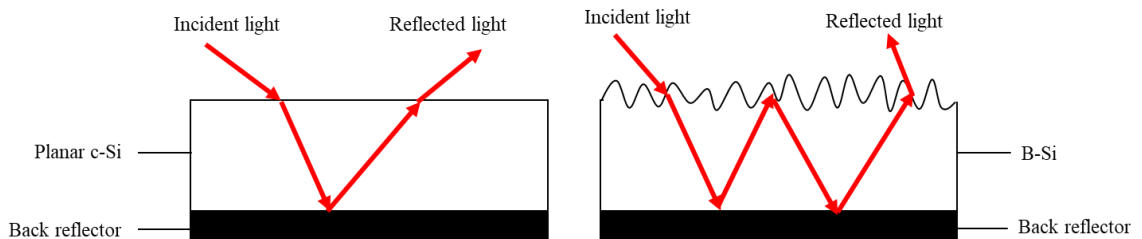


Figure 2.7 Optical path of incident light in planar c-Si (left) and b-Si (right). Note that the schematic diagram is not to scale.

## 2.4.1 Fabrication methods of black silicon

In this section, methods to fabricate b-Si are discussed. Fabrication of b-Si involves etching process, which requires controlled removal of c-Si from the original substrate (i.e. c-Si wafer) in order to form b-Si nanotextures. The methods used in the literature are divided into two groups; dry etching and wet etching.

### 2.4.1(a) Dry etching

Dry etching is a process where the etching is performed in a plasma environment. Reactive ion etching (RIE) is classified as a dry etching method. RIE process involves multi-cathode RF system (see Figure 2.8) which utilizes at least a combination of two types of gases to create radical species and to passivate the c-Si surface that has been etched. Generally, oxygen gas ( $O_2$ ) and sulphur hexafluoride ( $SF_6$ ) are used to create oxygen ( $O^*$ ) and fluorine ( $F^*$ ) radicals. The  $F^*$  radicals are used to etch the c-Si substrate. Later, the  $F^*$  radicals react with c-Si to form volatile products such as  $SiF_4$  which then reacts with  $O^*$  and a passivation layer is generated. This layer can be removed from the surface with further etching by  $F^*$  radicals (C. Hsu et al., 2014).

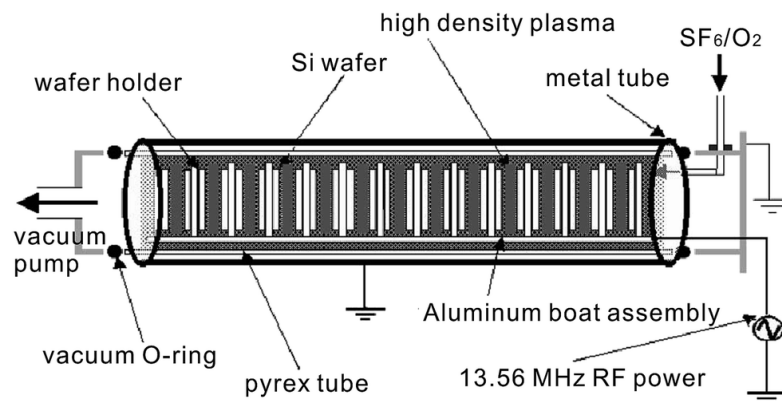


Figure 2.8 RIE process in a multi-cathode system (Liu et al., 2014).

Plasma immersion ion implantation (PIII) is also employed to perform the reaction of SF<sub>6</sub>/O<sub>2</sub> on c-Si. In this process, strong negative bias (-500 V) is applied to the wafer holder. The plasma is produced by radio frequency (RF) glow discharge. During this process, the reactive ions and radicals will be ionized from SF<sub>6</sub> and O<sub>2</sub> gases. The electrons are repelled from the holder due to the negative bias but positive ions are attracted and react with the c-Si substrate (Xia et al., 2011). Sometimes, SF<sub>6</sub> is also combined with chlorine (Cl<sub>2</sub>) gas to generate silicon tetrachloride (SiCl<sub>4</sub>) (Park et al., 2013). There are few combinations of gas mixtures which are common for the RIE process. This includes SF<sub>6</sub>/O<sub>2</sub> (Alshaltami et al., 2017; Tinck et al., 2017), SF<sub>6</sub>/C<sub>4</sub>F<sub>8</sub> (Zhu et al., 2015), SF<sub>6</sub>/O<sub>2</sub>/Cl<sub>2</sub> (Park et al., 2013) and SF<sub>6</sub>/O<sub>2</sub>/CHF<sub>3</sub> (Ye et al., 2015).

#### **2.4.1(b) Wet etching**

Synthesis of porous silicon was reported by using a chemical bath that contains HF, H<sub>2</sub>O<sub>2</sub> and HNO<sub>3</sub> without utilizing high temperature. But later, the wet etching method was extensively explored in detail. Wet etching is a process that utilizes wet chemical etchant to remove material. Metal-assisted chemical etching (MACE) method is classified as a wet etching process. MACE process is facile, requires simple setup and low-cost in nature (Yang et al., 2019) since mass production of PV cells is focusing on reducing the amount of material used and fabrication cost. This offers significant advantages over RIE process which requires vacuum processing and complicated setup. Besides, RIE is also more expensive since it requires state of the art processing equipment (Hou et al., 2020). MACE method is not only limited for c-Si, but it is also applicable for other semiconductor materials such as gallium arsenide (GaAs) (Cheung et al., 2014), silicon germanium (SiGe) (Wu et al., 2014) and gallium nitride (GaN) (Wang et al., 2016).

For the etching of c-Si via MACE process, it requires presence of metal nanoparticles (NPs) and chemical etching solution (HF and oxidizing agent). The porosity of c-Si produced by MACE process is dependent on the etchant concentration. There are two types of MACE; one-step and two-step MACE methods. Both of these step processes are carried out at room temperature. One-step MACE method is called direct etching as the metal NPs and etching process are carried out simultaneously when immersing the c-Si substrate in a solution containing of HF and metal salt such as  $\text{AgNO}_3$  (Huang et al., 2015; S. Li et al., 2014). On the other hand, two-step MACE method requires two separate processing steps; (i) metal deposition and (ii) chemical etching process. In the two-step MACE method, a metal catalyst (Au, Ag, Pt, Ni or Cu) (Cao et al., 2015; Deraoui et al., 2013; Zhong et al., 2013) are deposited first on c-Si substrate followed by chemical etching. The type of catalyst used in the process also influences the stability of the etching rate.

In this work, Ag has been chosen as a catalyst as it can significantly reduce the reflection of the c-Si to less than 10% within 300-1100 nm wavelength region, which is crucial for PV conversion process (Wang et al., 2013). The effects towards the MACE process can be tuned by changing the thickness of the Ag film and also the temperature of Ag annealing on the c-Si substrate. Usually, Ag thickness of 15 nm is used for the MACE process because it can generate well-distributed structure of Ag network at temperature of 200-250°C. If the thickness of the Ag film increases, it is increasingly difficult to produce nanopores on the c-Si after the MACE process even though the annealing temperature is high (about 300°C).

Various techniques can be used to deposit metal catalyst on the c-Si substrate such as electroless metallization, evaporation or sputtering (Liu et al., 2014). In order to form silicon nanopores or nanowires, the etching process involves a solution of HF

and an oxidizing agent. Note that the concentration of the etchant solution is very important because it can control the desired morphology of the nanopores or nanowires on the c-Si after the MACE process. Any oxidizing agent that has higher reduction potential than the c-Si is good to be used which includes H<sub>2</sub>O<sub>2</sub>, Na<sub>2</sub>S<sub>2</sub>O<sub>8</sub>, KMnO<sub>4</sub>, K<sub>2</sub>Cr<sub>2</sub>O<sub>7</sub> and EtOH (Balasundaram et al., 2012; Chartier et al., 2008; Z. Smith et al., 2013). However, H<sub>2</sub>O<sub>2</sub> is the best candidate because it enhances the porosification rate as the potential is higher than the Ag<sup>+</sup>. The standard potential reductions of H<sub>2</sub>O<sub>2</sub> and Ag are illustrated in Table 2.2.

Table 2.2 Standard potential reduction, E<sup>0</sup> of H<sub>2</sub>O<sub>2</sub> and Ag materials.

Materials	Standard potential reduction, E <sup>0</sup> (V)
H <sub>2</sub> O <sub>2</sub>	1.76
Ag <sup>+</sup>	0.80

#### 2.4.2 Mechanism of two-step metal-assisted chemical etching

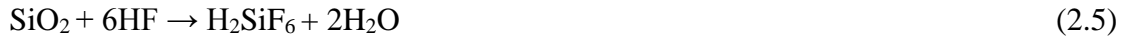
In two-step MACE process, the c-Si substrate is sputtered with Ag film followed by annealing to form Ag NPs before it is etched in an aqueous solution of HF:H<sub>2</sub>O<sub>2</sub>:DI H<sub>2</sub>O for a specific duration. The reaction during this process has been explained in (Abouda-Lachiheb et al., 2012; Hsu et al., 2014; Peng et al., 2008) as the following;

Cathode reaction (reduction of H<sub>2</sub>O<sub>2</sub>):



Anode reaction: Oxidation of Si and reaction of SiO<sub>2</sub> with HF





Overall reaction:



The Ag NPs are formed on the c-Si surface after annealing process. When the c-Si (with Ag NPs) is etched, the Ag NPs start catalyzing the reaction. The areas that are covered by the Ag NPs will be etched at a high rate (Wu et al., 2020). The Ag NPs are attracted to electrons from the c-Si and then the electrons are moved to  $\text{H}_2\text{O}_2$  for reduction reaction as shown in Equation 2.3. Since  $\text{H}_2\text{O}_2$  has higher positive electrochemical potential compared to c-Si, holes are easily injected into the c-Si. This reaction results in oxidation of c-Si during the anode reaction. When the c-Si is oxidized, Ag is provided with holes and electrons in Equation 2.4 which then transfers to  $\text{H}_2\text{O}_2$  for its reduction. Then,  $\text{SiO}_2$  is immediately produced as in Equation 2.5 and then etched away with HF to form pits as shown in Figure 2.9 (left). When the pits are formed, the Ag NPs are sunk into the pits as illustrated in Figure 2.9 (right). This reaction occurs continuously as long as there is  $\text{H}_2\text{O}_2$  for reduction process.

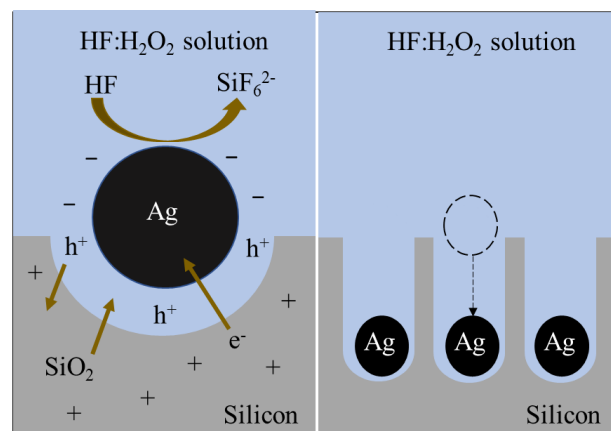


Figure 2.9 Mechanism of nanopores formation during two-step MACE process.

In the literature, b-Si has been produced by various methods for application in solar cells. A summary of these methods is depicted in Table 2.3. Note that all the methods below used Standard Test Conditions (STC) to evaluate the electrical performance of the b-Si solar cells. To date, the highest conversion efficiency of the b-Si solar cells has been realized by Savin et al., with 22.1% efficiency. In their work, the b-Si absorber was fabricated using deep reactive ion etching (DRIE) method (Savin et al., 2015). The b-Si surface was surface passivated with  $\text{Al}_2\text{O}_3$  using atomic layer deposition (ALD) process. This step is crucial in order to minimize surface recombination on the b-Si surface, which poses a larger surface area when compared to the planar c-Si reference (Song et al., 2020). Failure to effectively passivate the surface may cause the conversion efficiency of the b-Si solar cells to be poorer when compared to the planar c-Si solar cells.

Table 2.3 Electrical properties of b-Si solar cells synthesized by various methods.

Synthesis method	V <sub>oc</sub> (mV)	J <sub>sc</sub> (mA/cm <sup>2</sup> )	FF (%)	Efficiency (%)	Remarks	Reference
RIE	566	25.0	72	10.2	SiO <sub>2</sub> passivation	(Yoo et al., 2006)
RIE	564	28.6	73	11.7	SiO <sub>2</sub> passivation	(Yoo et al., 2006)
RIE	635	40.5	77	19.1	SiO <sub>2</sub> passivation	(Ingenito et al., 2015)
RIE	632	35.7	78	17.6	SiN <sub>x</sub> passivation	(Shim et al., 2012)
DRIE	665	42.2	78	22.1	Al <sub>2</sub> O <sub>3</sub> passivation	(Savin et al., 2015)
MACE	578	28.9	71	11.7	No passivation	(Srivastava et al., 2012)
MACE	628	36.5	79	18.2	SiO <sub>2</sub> passivation	(Oh et al., 2012)
MACE	623	35.6	78	17.1	SiO <sub>2</sub> passivation	(Zhao et al., 2014)
MACE	598	41.3	75	18.2	Al <sub>2</sub> O <sub>3</sub> passivation	(Wang et al., 2013)
MACE	636	37	80	19	SiN <sub>x</sub> passivation	(Li et al., 2020)
Femtosecond laser	507	39.2	72	14.1	SiO <sub>2</sub> / stacked layer passivation	(Iyengar et a., 2010)

## **CHAPTER 3**

### **METHODOLOGY**

#### **3.1 Introduction**

This chapter outlines the methods involved to synthesize b-Si and fabricate b-Si solar cells. Besides, the characterization equipments used to investigate surface morphological, optical and electrical properties of the b-Si and solar cells are also included in this chapter.

#### **3.2 Fabrication of black silicon**

In this work, two-step MACE method has been used to fabricate b-Si using p-type (100) wafer with resistivity of 1-10  $\Omega$ .cm. C-Si of (100) orientation is used because it exhibits high carrier mobility which is important for solar cell performance. In this method, Ag thin film (15 nm thickness) is sputtered on c-Si substrate, then annealed in a furnace at low temperature (200-260°C) for a brief duration (about 40min) in order to form random Ag NPs on the surface. After the annealing, the c-Si wafer is subjected to wet chemical etching process to turn c-Si into b-Si. The flow chart of the fabrication process is illustrated in Figure 3.1. The details for each process step are explained in the next section.

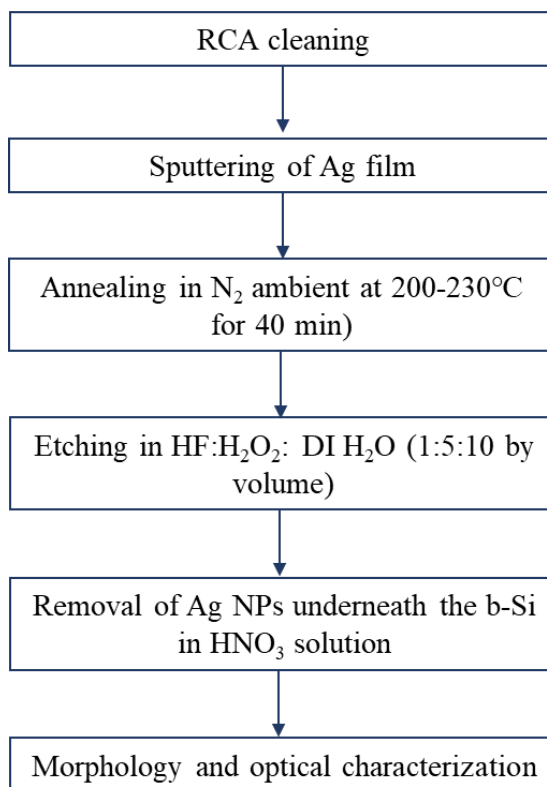


Figure 3.1 Flow chart of detailed procedures for the synthesis of b-Si.

### 3.2.1 RCA cleaning

Before proceeding to the two-step MACE process, 250  $\mu\text{m}$ -thick p-type monocrystalline silicon (mono c-Si) wafers with resistivity of 1-10  $\Omega\text{ cm}$  are cleaned using Radio Corporation America (RCA) technique to make sure that all contaminants are removed from the surface of the wafers. Three beakers labeled as 1, 2 and 3 are filled with different solutions. The steps of RCA cleaning are as follows:

- 1) Beaker 1: The c-Si wafers are placed into a heated Beaker 1 that contains solution of  $\text{H}_2\text{O}/\text{NH}_4\text{OH}/\text{H}_2\text{O}_2$  (5:1:1 by volume) for about 10 minutes. The temperature of the solution is controlled at 80°C. The purpose of this step is to remove the insoluble inorganic contaminants. Then, the wafers are rinsed with deionized water (DI  $\text{H}_2\text{O}$ ).

- 2) Beaker 2: The wafers are immersed in Beaker 2 with solution of HF/H<sub>2</sub>O (1:50 by volume) for 10 to 15 minutes. The purpose of this step is to remove native oxide on the c-Si wafer. Subsequently, the wafers are rinsed with DI H<sub>2</sub>O.
- 3) Beaker 3: The c-Si wafers are then soaked in Beaker 3 that contains H<sub>2</sub>O/HCl/H<sub>2</sub>O<sub>2</sub> solution (6:1:1 by volume) heated at 75°C for 10 minutes. The purpose of this step is to remove the ionic as well as heavy metal atomic contaminants. After that, the wafers are rinsed again with DI H<sub>2</sub>O for 10 minutes before proceeding to the next process.

### **3.2.2 RF sputtering**

In this work, radio frequency (RF) sputtering process (Model: Auto HHV 500 Sputtering Coater) is used to deposit Ag thin film on c-Si wafers. The RF sputtering system is shown in Figure 3.2 (a). Prior to the sputtering process, c-Si wafers are attached beneath the sample plate. Then, Ag target as source material and sample plate are loaded into the sputtering chamber as illustrated in Figure 3.2 (b). When the chamber base pressure reaches at  $4 \times 10^{-5}$  mbar, argon (Ar) gas of 9 sccm is filled into the chamber at room temperature. The shutter is opened and voltage is applied between the target and the substrates. Ar gas is ionized to form plasma (Ar ions). The Ar ions are bombarded at the Ag target and to sputter 15 nm Ag film onto the c-Si substrates. During the deposition, the sample plate is continuously rotated to ensure uniform deposition of Ag film on the surface of c-Si substrates. The parameters used for the deposition of Ag film is shown Table 3.1.

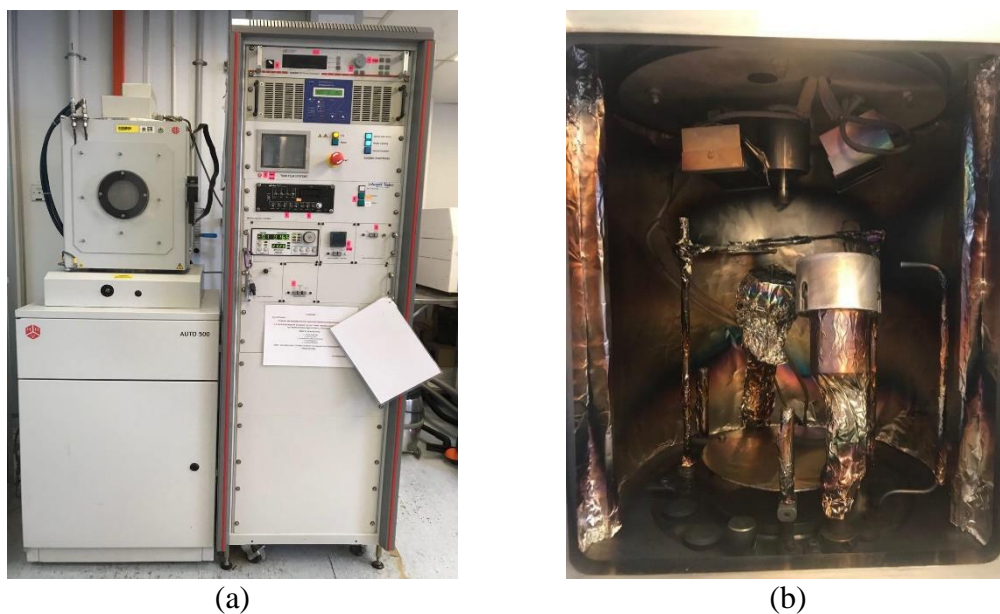


Figure 3.2 (a) Auto HHV 500 Sputtering Coater (b) Chamber of sputtering where the c-Si wafers are loaded.

Table 3.1 Parameters for the deposition of Ag thin film using RF sputtering.

RF power (W)	50
Thickness (nm)	15
Deposition rate ( $\text{\AA}/\text{s}$ )	1.1
Ar gas flow (sccm)	9
Temperature ( $^{\circ}\text{C}$ )	Room temperature
Chamber base pressure (mbar)	$4.0 \times 10^{-5}$
Working pressure chamber (mbar)	$3.5 \times 10^{-3}$

### 3.2.3 Annealing

Annealing is a heat treatment process performed in a furnace at a suitable temperature to produce Ag NPs on the c-Si wafers. The furnace used for annealing is shown in Figure 3.3. In this work, the c-Si wafers with Ag thin film are placed on quartz boat and pushed into the middle of the furnace when the temperature reached 200-260

°C (depends on annealing condition). The samples are annealed for an optimum temperature of 40 min in nitrogen ( $N_2$ ) atmosphere at flow rate of 2 L/min in order to form Ag NPs on the c-Si wafer (Pakhuruddin et al., 2017). The temperature range and duration have been shown to produce Ag NPs with average diameter of 100-200 nm which may be useful for the fabrication of b-Si with low broadband reflection. After the annealing process, the wafers are cooled before they are kept in a petri dish.

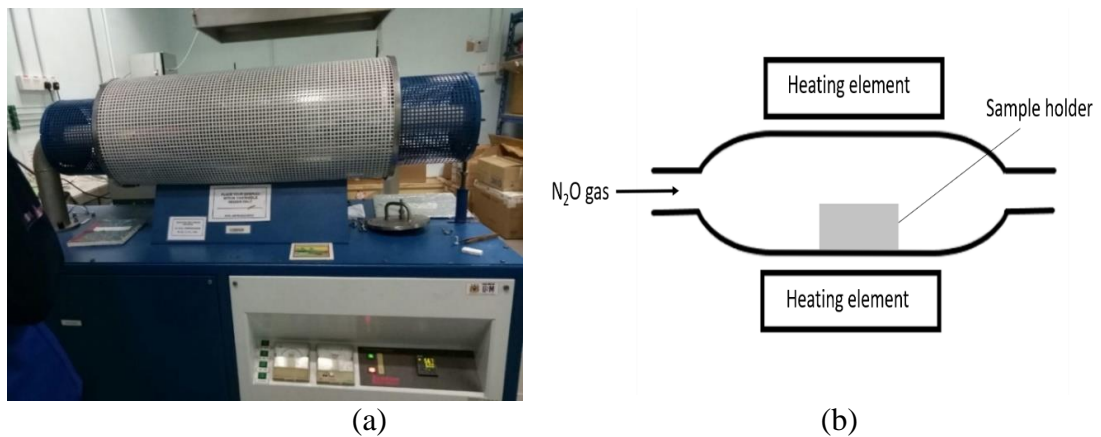


Figure 3.3 (a) Blue furnace for annealing process and (b) schematic configuration for thermal annealing.

### 3.2.4 Etching

After the annealing process, the c-Si (with Ag NPs on the surface) wafers are ready for etching process. The etching is conducted in a fume hood. In the fume hood, the etchant solution which is composed of a mixture of HF:H<sub>2</sub>O<sub>2</sub>:DI H<sub>2</sub>O is prepared (Otto et al., 2015). The total volume of the mixture is fixed at 160 ml and parameters such as concentration and volume ratio of HF, H<sub>2</sub>O<sub>2</sub> and DI H<sub>2</sub>O are varied from 1:5:10-5:1:10 volume ratio. In this process, the use of glass beaker is strictly prohibited since HF can etch the glass. So, teflon beaker must be used instead of glass beaker. The c-Si wafers are put on a Teflon holder before they are dipped into the etchant solution as